Theoretical Raman spectrum of boron carbide B4.3C under pressure

Antoine Jay, Olivier Hardouin Duparc, Jelena Sjakste, Nathalie Vast

Theoretical Raman spectrum of boron carbide $B_{4.3}C$ under pressure

Antoine Jay*
Laboratoire d'analyse et d'architecture des systèmes, CNRS, 31031 Toulouse cédex 4, France

Olivier Hardouin Duparc, Jelena Sjakste, and Nathalie Vast†
Laboratoire des Solides Irradiés, CEA/DRF/IRAMIS, École Polytechnique, CNRS, Institut Polytechnique de Paris, 91120 Palaiseau, France

The most striking features of the Raman spectrum of boron carbide under pressure are explained theoretically by computing the Raman tensor using density functional perturbation theory and the second-order response. While the observed pressure-induced changes in frequencies and intensities of all of the peaks above 450 cm^{-1} are convincingly explained by the vibrations of ($B_{11}C$) icosahedra and C-B-C chains - that have been identified for long as the two main components of the atomic structure of pristine B_4C -, the puzzling non-monotonic behavior of a broad Raman band at low frequency, whose intensity increases under pressure up to 44 GPa, decreases and then vanishes, was so far unexplained. We find that the behaviour under pressure of both the frequency and intensity of this band turns out to be remarkably accounted for, in the calculations, by the activation of the chain bending mode in atypically flexured chains. We show that the flexion of the chain occurs at high pressure in presence of interstitial B atoms that, at ambient pressure, sit in the prolongation of standard C-B-C chains. We propose the ambient-P mode observed at 270 cm^{-1} as a fingerprint for the identification of both such B-C-B-C chain-defects in boron carbide and local deviations from the rhombohedral symmetry.

PACS numbers: 78.30.-j 63.20.-e 63.20.D-

I. INTRODUCTION

Boron carbides are semiconducting materials well known for their remarkable properties such as their large electronic band gap, their ability to absorb neutrons, and their high values of the melting temperature, bulk modulus, hardness and Hugoniot elastic limit, specially for atomic carbon (at. C) concentrations close to 20% [1]. However, despite decades of investigations, the nature of disorder in samples of boron carbide is still a matter of debate. The ordered theoretical ground state at 0 K is found to be the monoclinic ($B_{11}C^p$)C-B-C atomic structure (figure 1a), composed of ($B_{11}C^p$) icosahedra linked together directly through their polar sites (p), and indirectly though C-B-C chains bonded to their equatorial sites (e) [1–4]. However, the 20% at. C concentration phase, known as B_4C^p, which has by far the lowest formation enthalpy in the density functional theory (DFT), has never been reached experimentally [5]. Instead, the maximum carbon concentration in the so-called homogeneity range observed in the phase diagram (which is known only above 1000° C) [6], is ≈ 18.8%, leading to the $B_{4.3}C$ stoichiometry [5]. The fact that the maximum reachable concentration is not the one theoretically obtained at 0 K suggests that, with respect to B_4C^p, some changes in the icosahedral and chain building blocks take place at high temperature.

The unknown $B_{4.3}C$ structure can only be synthesized at high temperature. It apparently remains unchanged while cooling down the samples to the ambient temperature, possibly because of very large kinetic barriers that stabilize high temperature configurations. For instance, occurrence of the polar substitutional disorder, called *6P* disorder, where the carbon atom in each ($B_{11}C^p$) icosahedron is statistically distributed among the 6 equivalent polar positions, is expected at finite T and leads to the $R\bar{3}m$ symmetry [3, 4, 7].

Other configurations that modify the stoichiometry have also been proposed: some ($B_{11}C$) icosahedra can be replaced by (B_{12}) [8] or ($B_{10}C_2$) [9] ones, and/or some C-B-C chains can be replaced by the linear B-C-B-C [10] (figure 1b), the pantographic $C\langle{}^{B}_{B}\rangle C$ [11] (figure 1c) or $B\langle{}^{B}_{B}\rangle B$ [12] (figure 1d) configurations, where $\langle{}^{B}_{B}\rangle$ stands for two interstitial atoms in the Wyckoff site of the average rhombohedral structure [13]. Beside the modification of the chain itself, the three latter defects also involve the modification of three neighboring icosahedra, which are (B_{12}) instead of ($B_{11}C$). They will nonetheless be called "chain-defects" in the following, for simplicity. In addition, other chain defects like the C-B-B [15], C-C [16] and C□C [17] chains, where □ stands for vacancy, have also been proposed.

Interestingly, $B\langle{}^{B}_{B}\rangle B$ and C-B-C-B chains have been observed by high-resolution transmission electron microscopy [10] (HRTEM). Moreover, they have been shown to have the lowest DFT formation energy in ordered structures of 414 atoms, at respectively the 8.7% and 13.04% at. C concentrations, thus defining the theoretical convex hull at 0 K [13]. It is then highly probable that at least one of these building blocks is present in the $B_{4.3}C$ structure, however, the identification of such defects by spectroscopic means supplemental to HRTEM

* antoine.jay@laas.fr
† nathalie.vast@polytechnique.edu

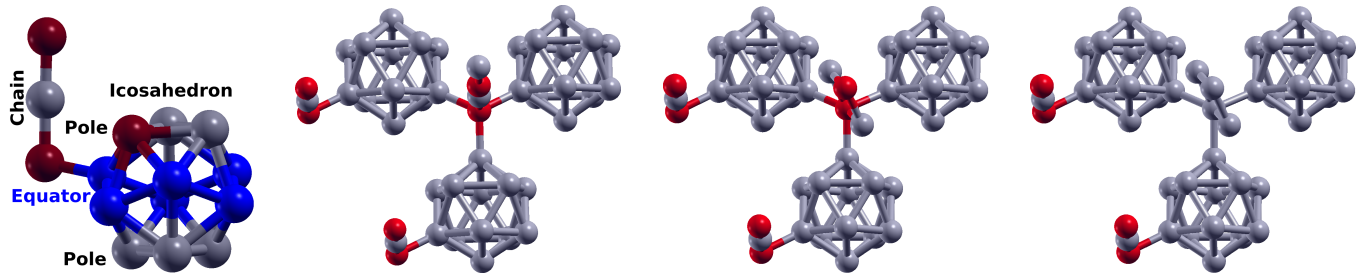

(a) B_4C unit cell c=20% $E_{>hull}$=0.0 meV/at.

(b) B-CBC +$3B_{12}$ defect c=19.21% $E_{>hull}$=1.0 meV/at.

(c) $C\langle^{B}_{B}\rangle C$ +$3B_{12}$ defect c=19.21% $E_{>hull}$=1.6 meV/at.

(d) $B\langle^{B}_{B}\rangle B$ +$3B_{12}$ defect c=18.72% $E_{>hull}$=2.5 meV/at.

FIG. 1. Atomic structures of B_4C (panel a) and of the three complex defects that have the lowest formation energy when introduced in a supercell of B_4C: the C-B-C-B chain [14] (panel b); the pantographic $C\langle^{B}_{B}\rangle C$ [11] (panel c); the pantographic $B\langle^{B}_{B}\rangle B$ [12] (panel d). Grey and blue balls: boron atoms. Red balls: carbon atoms. c is the carbon concentration in the 3×3×3 supercell and $E_{>hull}$ the formation energy of the supercell with respect to the formation energy of the convex hull at c [11, 13]. The other chain defects studied in the present work are not illustrated.

and DFT is still lacking.

In fact, due to its high precision, Raman spectroscopy has also been used under high hydrostatic pressure to try and unveil the atomic structure of $B_{4.3}C$, with however limited success. The measurements that have been performed up to respectively 36 GPa [18], 50 GPa [19] and 70 GPa [14, 20] have shown that: *(i)* A peak appears above 20 GPa around 1000 cm^{-1} (marked as "appearing peak" in figure 2, and highlighted by the orange dashed box in figure 3); *(ii)* The two narrow, harmonic, peaks at 480 cm^{-1} and 580 cm^{-1}, which are characteristic of boron carbide at ambient pressure and enable one to identify B_4C in polyphased samples [21], are also present at any pressure; They are respectively induced by the chain rotation and by the icosahedral libration [3, 4] named *pcr* and *lib* in figure 3; *(iii)* All of the frequencies above 450 cm^{-1} have positive monotonic Grüneisen coefficients throughout the whole pressure range.

In wide contrast, a broad Raman band at low frequency has an intensity which increases up to 44 GPa, decreases and then vanishes (figure 3). This band, which we call the "low frequency band", is dominated under pressure by a peak initially at 270 cm^{-1}, whose frequency remarkably decreases down to 212 cm^{-1} at 44 GPa, increases above 44 GPa and then remains constant (figure 2). The origin of this band has so far remained unexplained [22, 23], despite several suggested hypotheses like surface effects [24], the activation of the infrared active C-B-C chain libration modes observed at the same frequency [24], the presence of the pantographic $B\langle^{B}_{B}\rangle B$ [25] or C-B-B [26] defects. As we will show, none of these hypotheses can explain the non-monotonic behavior under pressure of the low frequency band. To summarise, Raman spectra of boron carbides under pressure in general, and the low frequency band in particular, are presently the subject of very active debates [22, 23, 26–29], due to their crucial importance for the understanding of the phase diagram of boron carbides.

Turning to theory, Raman spectra can nowadays be computed with an extremely high reliability with *ab initio* methods in high performance computing environments (HPC), and enable a straightforward interpretation of the (complex) experimental results, through the comparison not only of the measured mode frequencies and intensities, but also with their variation with pressure. In the present work, the theoretical Raman spectra of $(B_{11}C^{p})$C-B-C in presence of each of the above-mentioned defects have been calculated from 0 to 70 GPa and compared to the experimental spectra. We show that all of the high frequency modes, including the peak appearing around 1000 cm^{-1}, are remarkably explained by lattice vibrations of the $(B_{11}C^{p})$C-B-C ordered ground state. We show moreover that the behavior under pressure of the low frequency band can only be explained by a bending mode of atypically flexured-chains, and that the atypical flexion occurs in presence of an interstitial boron atom, leading to B-C-B-C chain defects at ambient pressure that undergo a flexion under pressure (figure 1b). Therefore, the main text of this paper mainly focuses on the B-C-B-C defect, while the results for other defects are presented in the appendix A ~~and B~~.

The technical details of the modeling and of the calculations are presented in section II with complements in appendix ~~B and~~ B. The resulting Raman spectra at different pressures are reported in section III. The behaviour under pressure of the Raman peaks that are present in undefective B_4C are analysed in paragraph III A, with details in appendix ~~E and~~ C. The low frequency band, which turns out to be induced by the B-C-B-C defect, is presented in paragraph III B, with detailed given on its Grüneisen coefficients in paragraph III C. Conclusions are drawn in section IV.

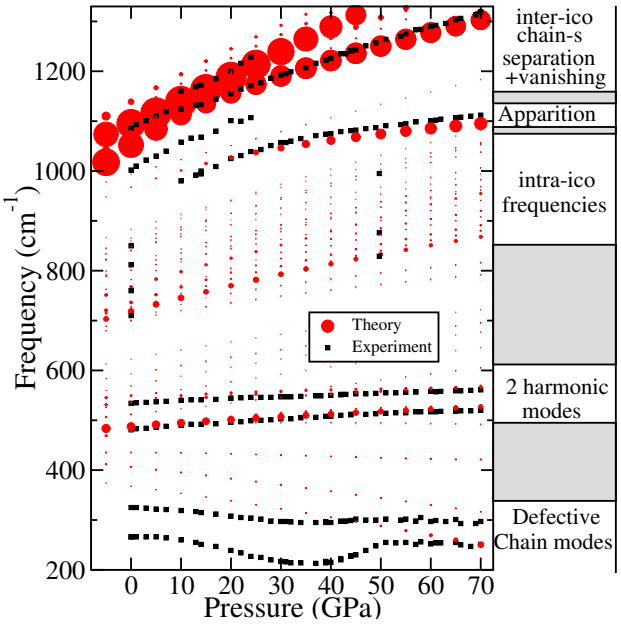

FIG. 2. Vibrational frequencies of B_4C^p as a function of pressure for the 15-atom ordered monoclinic ground state, $(B_{11}C^p)$C-B-C calculated within DFPT-LDA and the second order response. The area of the red disks is proportional to the theoretical Raman intensity. Experiments on $B_{4.3}C$ from Ref. 14. $intra-ico$: intra icosahedral vibration. $inter-ico$: inter icosahedral. $chain-s$: chain stretching. In the Cm space group, all the vibrational modes are in principle Raman active, with however a small intensity for the ones that correspond to IR active modes in the $R\bar{3}m$ space group, which explains the red disks with a small area. Details can be found in Ref. 30.

II. METHODS

A. Structures details

In this work, we have considered defective chains such as C□C, C-C, C-B-B, B-C-B-C, C-C-B-C, the $B\langle{}^{B}_{B}\rangle B$ pantograph, or the $C\langle{}^{B}_{B}\rangle C$ pantograph. The Raman spectra of B_4C with one such defect have all been calculated in 3×3×3 supercells containing between 404 and 406 atoms, depending on the studied defect. The monoclinic $(B_{11}C^p)$C-B-C building block presented in figure 1a has been used 27 times. When the supercell is defined as ordered, the substitutional position of the carbon atom in the icosahedron is the same from one icosahedron to the other. On the contrary, in $6P$-disordered supercells, the position of the substitutional carbon atom in the icosahedron has been varied from one icosahedron to the other, so that the distribution of substitutional carbon atoms is homogeneous in the supercell and avoids C-C bond formation that would increase the internal energy [7, 23]. After relaxation of the lattice parameters of the supercell, $6P$-disordered supercells have on average rhombohedral cell parameters and an average $R\bar{3}m$ space group. In fact, as one can see table I, the magnitude of the distortion with respect to the rhombohedral average is much smaller in $6P$ disordered supercells than in ordered ones. The $6P$ disorder is thus a useful means to approach the rhombohedral symmetry in the calculations.

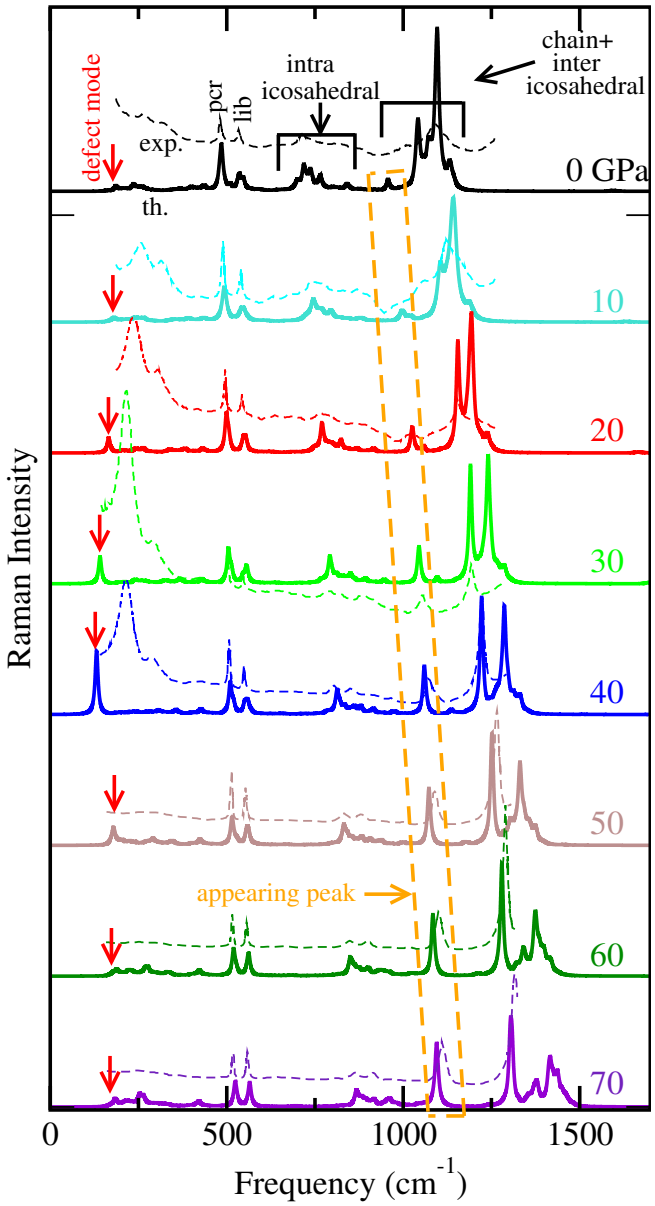

FIG. 3. Theoretical Raman spectra between 0 and 70 GPa for the B-C-B-C defect $(B_{11}C^p)_{24}(B_{12})_3$(C-B-C)$_{26}$(B-C-B-C)$_1$ (solid line). Experimental Raman spectra of $B_{4.3}C$ from Ref. 14 (dashed line). Calculations performed in a 3×3×3 ordered supercell.

To create the chain defect, the C-B-C chain in the center of the supercell has been replaced by one of the above-mentioned defective chains, whereas the surrounding $(B_{11}C^p)$ icosahedra have been changed to (B_{12}) or $(B_{11}C^p_2)$ ones in order to fulfill the Wade rule [31], which ensures that the defective boron carbide is still a semi-

Structure	N_{at}	$E_{>hull}$	c	a_r	α_r	Fig.
Ordered elemental unit cell						
B_4C^p	15	0	20	5.10±0.10	65.79±0.59	2
$(B_{10}C^pC^e)$C-B-B	15	37.3	20	5.09±0.14	66.17±1.17	10
Defect in ordered B_4C^p						
$B\langle^B_B\rangle B{+}3(B_{12})$	406	2.5	18.72	15.30±0.26	65.83±0.50	8a
$C\langle^B_B\rangle C{+}3(B_{12})$	406	1.6	19.21	15.30±0.26	65.82±0.51	X
B-C-B-C+3(B_{12})	406	0.8	19.21	15.30±0.27	65.73±0.56	3
C-C-B-C+4(B_{12})	406	7.2	19.21	15.31±0.27	65.82±0.52	8b
Defect in 6P disordered B_4C^p						
No defects	405	9.5	20	15.29±0.00	65.79±0.00	9,8c
$B\langle^B_B\rangle B{+}3(B_{12})$	406	11.7	18.72	15.30±0.00	65.85±0.03	X
$C\langle^B_B\rangle C{+}3(B_{12})$	406	11.5	19.21	15.31±0.01	65.74±0.13	8e
B-C-B-C+3(B_{12})	406	11.3	19.21	15.31±0.01	65.82±0.02	12
(B_{12})C-B-B	405	13.3	19.51	15.29±0.03	65.86±0.03	8d
(B_{12})C□C	404	12.1	19.80	15.29±0.00	65.77±0.00	8f
C-C-B-C+4(B_{12})	406	16.3	19.21	15.31±0.01	65.83±0.02	X
C-C intra-ico	405	11.5	20	15.29±0.00	65.81±0.00	9
C-C inter-ico	405	12.4	20	15.29±0.00	65.80±0.00	9
($B_{10}C^p{}_2$)C-C	404	13.4	20.30	15.25±0.00	65.91±0.00	9

TABLE I. Modeling parameters of the defects and reference to their Raman spectrum (last column). N_{at} is the number of atoms in the ordered or *6P*-disordered supercell. $E_{>hull}$ is the formation energy (meV/at) calculated with respect to the convex hull of the formation energy [11, 13] at the given atomic carbon concentration c (%) at 0 K and 0 GPa. a_r and α_r are respectively the average rhombohedral lattice parameter (Å) and angle (°) of the three supercell vectors. The numbers with ± sign represent the magnitude of the distortion in the supercell with respect to the rhombohedral average. The numbers in last column refer to the figures (figure numbers) representing corresponding Raman spectra, present in the main text of the present work, or in appendix A, X corresponding to no figure present.

conductor and avoids half-filled orbitals. This means that each chain defect with excess electrons must be in the vicinity of electron-deficient icosahedra, given that: the arachno (B_{12}) is deficient by two electrons, ($B_{11}C$) by one electron and ($B_{10}C_2$) is not deficient, while the C□C chain has two excess electrons, C-B-C has one excess electron and the C-C and C-B-B chains do not have any excess electron. The B-C-B-C chain, $C\langle^B_B\rangle C$ and $B\langle^B_B\rangle B$ pantographs are particular cases: each of them stabilizes 3 neighboring (B_{12}) icosahedra (figures 1d, 1b, and 1c).

We note that there are many possible combinations of positions in which the (B_{12}) can be linked to the defective chain: all of them lead to a semi-conducting material and the conclusions of the present work do not depend on the particular combination. In our model, the combination of (B_{12}) positions that is used is the one that has the lowest formation energy (figure 1 and table I). We point out that the electron neutrality can also be achieved by adding charges into the system [11].

B. Computational details

Total energy calculations have been performed using the density functional theory (DFT) [32, 33] in the local density approximation (LDA) [34] as implemented in Quantum ESPRESSO [35]. A shifted Monkhorst-Pack grid of 2^3 **k**-point has been used to sample the Brillouin zone (BZ) [36]. The size of the plane wave basis set has been limited with a cutoff energy of 80 Ry. All the lattice parameters and atomic positions have been relaxed. Second-order force constants have been calculated within density functional perturbation theory (DFPT) [37] at the BZ center (Γ) in order to obtain the frequencies ω and eigenmodes of the dynamical matrix. All the studied structures are semi-conducting, which allows for the evaluation of the Raman tensor $\overleftrightarrow{A}$ using the second order response [38] (Appendix B).

Each Raman spectrum has been calculated at eight different pressures, in the range between 0 and 70 GPa. This enables the evaluation of the slope of each frequency ω as a function of the pressure P, known as the Grüneisen coefficient and defined as $\gamma = -\frac{V}{\omega}\frac{\partial\omega}{\partial V}$, where V is the unit-cell volume. It has been calculated by finite difference of the frequency $\omega(P)$ at $P-10$ GPa and $P+10$ GPa.

III. RESULTS

Remarkably, among all the defects computed in this study, only the B-C-B-C chain with three surrounding (B_{12}) icosahedra (figure 1b) accounts for the experimentally observed non-monotonic behaviour of low-frequency peaks under pressure varying between 0 and 70 GPa (figure 3).

Indeed, a peak appears around 187 cm^{-1} when pressure is increased (indicated by red arrows in figure 3). The intensity of this last peak reaches a maximum at 40 GPa, and then decreases beyond 40 GPa. Characteristics of this defect-mode with non-monotonic behaviour under pressure are detailed in table II (right hand side), and will be discussed further below.

The second noticeable feature is that a peak around 1000 cm^{-1} appears under pressure, in the sense that its intensity drastically increases with increasing pressure (see the area in orange dashed box in figure 3). The appearance of the high-frequency peak is a property of non defective boron carbide ($B_{11}C^p$)C-B-C, as we find the same appearing peak in the simple calculation with 15-atoms (figure 2).

Calculations of figure 3 are our main result and account for all of the experimental observations. In the following, we first discuss the high-frequency part of the Raman spectra, and in particular the origin of the peak around 1000 cm^{-1}. Then we will show that the peak around 187 cm^{-1} is due to the B-C-B-C chain defect.

Pressure		Intra-I Eq-Eq	Intra-I Pol-br	Intra-I Eq-br	Inter-I Sym	Chain Sym
0 GPa	ω_{th}	719	699	994	1071	1096
	γ_{th}	1.01	1.30	0.76	1.32	1.00
50 GPa	ω_{th}	833	841	1074	1336	1250
	γ_{th}	0.91	1.02	0.44	1.38	0.90

(a) (b) A_{1g}

		lib	*pcr* Eq-Ch	Intra-I Pol-Eq	Intra-I Eq-Eq	Intra-I Pol-Eq2	Inter-I Asym	Chain Rot
0 GPa	ω_{th}	536	488	768	841	815	1042	1131
	γ_{th}	0.37	0.40	1.09	0.97	0.94	1.36	1.28
50 GPa	ω_{th}	562	517	885	995	927	1308	1359
	γ_{th}	0.37	0.39	0.89	0.96	0.91	1.20	1.21

(c) E_g

		B-C-B-C bending
0 GPa	ω_{th}	187
	γ_{th}	-0.3
50 GPa	ω_{th}	179
	γ_{th}	4.8

(d) Defect

TABLE II. Raman active frequencies ω (cm^{-1}) and their Grüneisen coefficient γ calculated at 0 and 50 GPa. $Intra-I$: intra icosahedral vibration (vib). $Inter-I$: inter icosahedral vib. *Pol*: polar atom vib. *Eq*: equatorial atom vib. *Chain*: chain mode. *Sym*: symmetric. *Asym*: anti-symmetric. *lib*: libration of the icosahedra. *pcr*: pseudo chain rotation. *br*: breathing mode.

A. Analysis of the high-frequency spectrum

In this section, we focus on the interpretation of the the Raman spectra for frequencies above 450 cm^{-1}, *i.e.* all the peaks at the exclusion of the defect peak (low frequency mode). In fact, the analysis of the high-frequency part of the Raman spectra does not require the introduction of any defects or disorder: the calculated Raman peaks are common to all of the supercells studied in this work (see appendix A, figures 8 and 9), as they originate from the $(B_{11}C^p)$C-B-C "building-block" which is present more than 24 times in each 3^3 supercell we have considered.

The progressive appearance of the peak around 1000 cm^{-1} (orange dashed box in figure 3) is due to the mode which is called the "breathing" of the hexagons formed by the six equatorial atomic positions (labeled "Eq-br" in table II and represented at 0 GPa ~~in appendix E,~~ figure 4a). The symmetry is A_{1g}, the intensity is quasi-zero at ambient condition, increases with pressure mainly above 20 GPa. This is explained by the fact that the pressure drastically reduces the distance between the equatorial atoms and the chain ends, so that the "breathing" of the hexagon leads to an interaction with the chain (see the mode at 60 GPa ~~in appendix E,~~ figure 4b), which induces a small chain stretching known to be highly Raman-active. As the stretching increases with pressure, the Raman intensity of the mode increases.

The Grüneisen coefficients of the 5 A_{1g} and 7 degenerated E_g modes are presented in table II at 0 and 50 GPa. They range from 0.33 for the icosahedral libration to 1.36 for the intericosahedral stretching modes (table II). Such a wide range of pressure coefficients can be explained by the fact that all the bonds do not contract in the same way under pressure (see Appendix C).

B. Description of the defect mode

In the following, we focus on the low frequency peak induced by the defect mode. This mode mainly corresponds to the vibration of the boron atom in the center of the C-B-C chain in the presence of an interstitial B atom, in the plane perpendicular to the chain direction (green arrows in figure 5), which creates a dynamical bending of the chain, known as the "bending mode" [39].

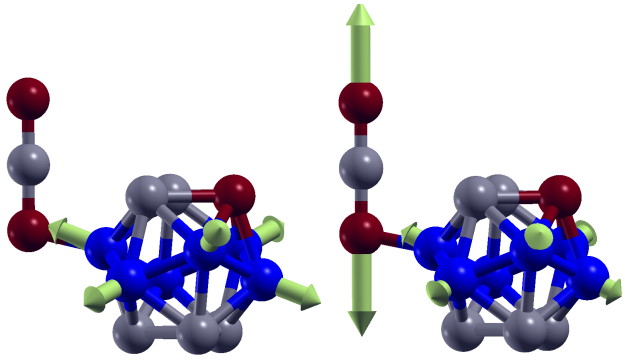

(a) 0 GPa, 994 cm^{-1}, Small Raman activity (b) 60 GPa, 1074 cm^{-1}, High Raman activity

FIG. 4. Atomic displacement (green arrows) induced by the A_{1g} eigenmode around 1000 cm^{-1} called the "breathing" of the equatorial atoms (blue balls). The displacement is transferred to the carbon atoms at the chain ends under pressure.

The vibration induced by the B-C-B-C chain defect has a low frequency and a Grüneisen coefficient that is negative at 0 GPa and positive at 50 GPa (table II). This is in wide contrast with all of the other modes for which the sign of the Grüneisen coefficients are similar at 0 GPa and 50 GPa.

The non-monotonic slope of the low frequencies observed experimentally is remarkably accounted for by the theory (figure 6, top panel). In particular, the ratio of the frequencies at finite pressure to the frequency at ambient pressure (in the expt.) or at 0 K (in the theory) are extremely close in the theory and experiment (figure 6, insert panel) even though a slight shift of the absolute frequency is found in the calculations. As shown in Appendix D, this shift is reduced by changing the type of defect in the chain, with an interstitial carbon instead of

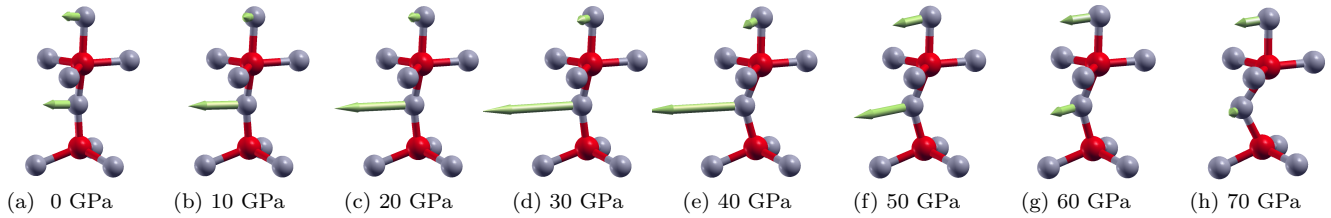

(a) 0 GPa (b) 10 GPa (c) 20 GPa (d) 30 GPa (e) 40 GPa (f) 50 GPa (g) 60 GPa (h) 70 GPa

FIG. 5. Evolution of the B-C-B-C + 3(B_{12}) defect atomic structure and of its eigenmode from 0 to 70 GPa in the ordered supercell. The green arrows indicate the eigenmode of the defect that becomes Raman active in the low frequency domain . Their size is proportional to the intensity of the eigenmode displacement. To avoid perspective misleading, the angles in the chain and the size of the arrow are also given in figure 7 (top panel).

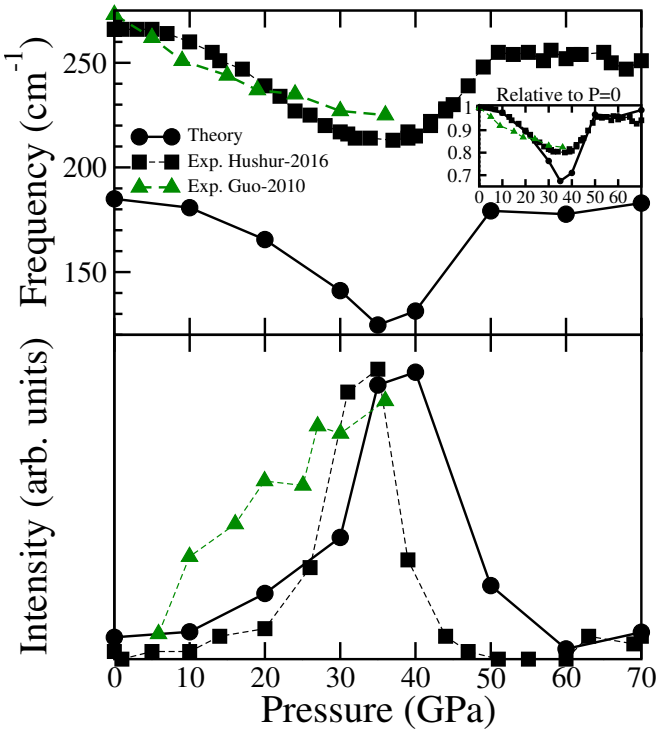

FIG. 6. Theoretical Raman frequencies (top panel) and intensities (bottom panel) induced by the B-C-B-C + 3(B_{12}) defect in the ordered supercell. Experiments Refs. [18] (green triangles) and [14] (black squares). The inset represents the experimental and theoretical frequencies relative to their respective value at ambient pressure.

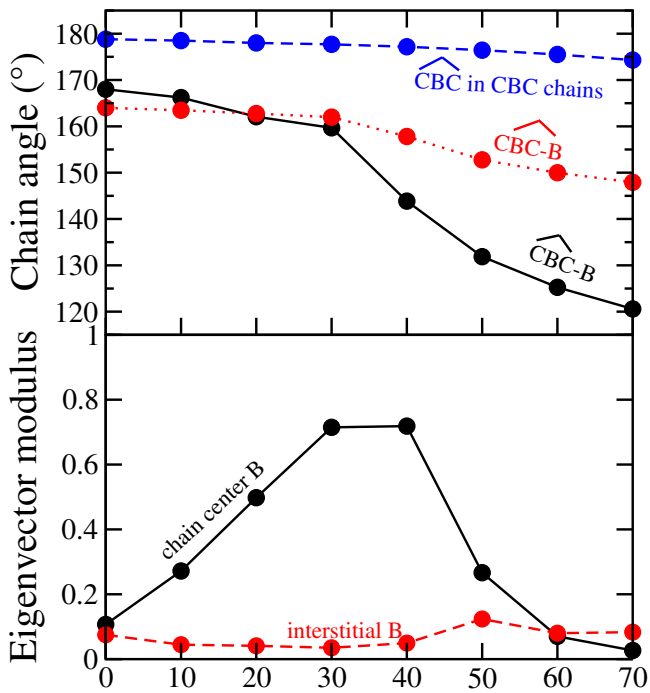

FIG. 7. Chain angle (top panel) and eigenvector modulus (bottom panel) as a function of pressure in the ordered supercell. The modulus represents the ratio of the size of the displacement of the interstitial boron atom (dashed red line) and of the boron atom in the center of the chain (black solid line) (as represented figure 5) by the total eigenvector displacement. The evolution of the C-B-C chain angle is also given.

the interstitial boron atom for instant, *i.e.* C-C-B-C. We find that the defect mode intensity is significant in the ordered supercell, and weak in the 6P disordered supercell (appendix D, figure 12), hence, some local distortion from the rhombohedral symmetry is necessary for the defect mode to be observed. We expect that, for steric reasons, any three-atom linear chain with an interstitial atom of any kind in its prolongation has the same behavior under pressure, *i.e.* undergoes a static flexion of the chain that activates the dynamical bending mode. Also in excellent agreement with the experiments, the mode becomes progressively Raman active with a maximum intensity at 40 GPa, and then becomes inactive for bigger pressures (figure 6, bottom panel).

We thus conclude that Raman spectroscopy provides a crucial means to detect B-C-B-C chain-defects in boron carbide and also to detect local distortions and deviations from the observed rhombohedral symmetry. It can be

considered as a help in controlling the amount of such defects in boron carbide.

C. Reason explaining the change of the Grüneisen coefficient

The non-monotonic behavior can be understood with the help of the pressure-induced variation of B-C-B-C chain geometry (figures 5 and 7). As one can see in figure 7, the presence of the additional atom in the intericosahedral space changes the geometry of the chain from linear at ambient pressure to flexured at higher pressure. This is due to the additional atom that prevents the intericosahedral volume reduction. Instead, the reduction of volume occurs through the flexion of the B-C-B-C chains that mainly starts above 40 GPa. Contrastingly, the "standard" C-B-C chains remain linear at any pressure (figure 7, blue dashed curve). Below 40 GPa, the B-C-B-C chain is only slightly non-linear (black solid curve) and its dynamical bending mode has a negative Grüneisen coefficient, as the one of standard C-B-C chains (Fig. 2). On the contrary, above 40 GPa, the B-C-B-C chain is no more linear and its bonds then shrink in the same way as for the other modes, implying a positive Grüneisen coefficient for the bending mode.

IV. CONCLUSIONS

In conclusion, we have computed the Raman spectra of boron carbide under high pressure, and demonstrated that most of the observations concerning the Raman spectra of $B_{4.3}C$ at different pressures can be nicely explained by lattice vibrations of the atomic structure of bulk pristine (B_4C^p). Moreover, we have shown that the presence of interstitial boron atoms induces a chain flexion under pressure which remarkably explains the observed non-monotonic change in slope and intensity of the low frequency band under pressure, provided the environment has a local distortion. For the first time, this offers an explanation that successfully encompasses all the key characteristics of the spectroscopic measurements, precisely aligning with the $B_{4.3}C$ concentration observed.

We have found that while other kinds of chain defects are possible contributors to the low frequency band, none of them shows the unusual variation of frequency and intensity under pressure. We thus conclude that Raman spectroscopy provides a crucial means to detect B-C-B-C chain-defects in boron carbide, and to identify local deviations from the rhombohedral symmetry.

ACKNOWLEDGMENTS

The authors thank Guido Roma for useful discussions. ~~Calculations have been performed with the QUANTUM ESPRESSO computational tool~~ [35]. This work has been granted access to HPC resources by the Partnership for Advanced Computing in Europe (PRACE Project No. 2019204962), the French HPC centers GENCI-IDRIS, GENCI-CINES and GENCI-TGCC (Project 2210), by the École Polytechnique through the 3L-HPC project, and by the Calmip (Project No. 1418). Financial supports from the ANR (BCSi project), the DIM SIRTEQ (région Île de France), and the DGA (France) are gratefully acknowledged.

Appendix A: Raman spectra of other defects

We present the theoretical Raman spectra of defects whose low frequency part cannot explain the experimental data (figure 8). The main features of their atomic structure are described in table. I.

Raman spectra have been computed for pressures varying from 0 to 70 GPa in *6P*-disordered supercells for the pantographic $B\langle\substack{B\\B}\rangle B$ and $C\langle\substack{B\\B}\rangle C$ chains, the linear B-C-B-C, C-B-B and C□C chains under pressure varying from 0 to 70 GPa. These chain defects are known to have a low formation energy (table. I). The Raman spectra have new peaks at low frequency, however the behavior of these peaks under pressure cannot explain the observed low-frequency band.

Other common defects with a higher formation energy [30] are presented in figure 9 only at 0 GPa, because no significant new peaks were distinguishable: inter and intra icosahedral C-C bonds with *6P* disorder, and the C-C chain near a ($B_{10}C_2$) icosahedron.

The non-monotonic behavior has also been obtained in the 15 atoms unit cell of ($B_{10}C^pC^e$)C-B-B as presented in figure 10. We find that the flexion of the C-B-B chain under pressure (not shown) increases the Raman intensity of the C-B-B dynamical bending eigenmode, and that the Grüneisen parameter becomes negative and then positive, like for the B-C-B-C defect. However, the reduction of the Raman intensity is not observed above 40 GPa for this structure. Moreover, the non-monotonic behavior is not recovered when this atomic structure is placed in a ($B_{11}C^p$)C-B-C matrix to simulate the isolated defect. this is due to the fact that, when the defect is isolated, the unit cell volume is similar to the one of B_4C. This hinders the flexion of the three-atom chains under pressure.

Appendix B: Raman analysis

A $R\bar{3}m$ 15-atoms unit cell of B_4C has 5 A_{1g} and 7 degenerated E_g Raman active modes. However, in the 3×3×3 supercells used here, the presence of the defect leads to a reduction of their symmetries and hence to slight shifts of the frequencies between each of the 15-atom building blocks. For this reason, there are 5×27 quasi A_{1g} and 7×27 quasi E_g modes that are Raman active, forming a total of 5+7 main peaks, each of them

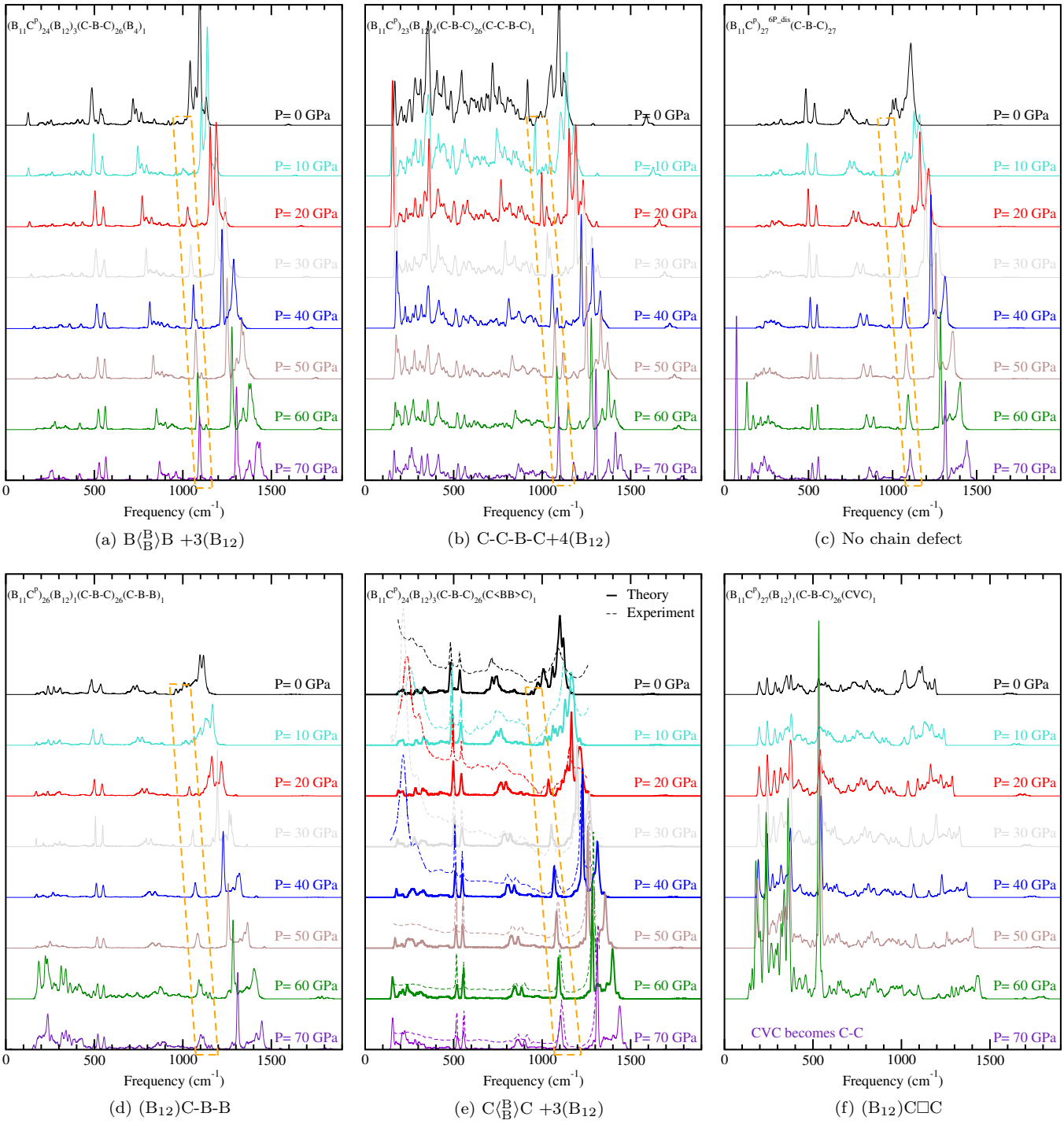

(a) B⟨$^{\mathrm{B}}_{\mathrm{B}}$⟩B +3($B_{12}$) (b) C-C-B-C+4($B_{12}$) (c) No chain defect

(d) (B_{12})C-B-B (e) C⟨$^{\mathrm{B}}_{\mathrm{B}}$⟩C +3($B_{12}$) (f) ($B_{12}$)C□C

FIG. 8. Theoretical Raman spectra of the 3×3×3 rhombohedral supercell ($B_{11}C^p$)C-B-C from 0 to 70 GPa containing various kinds of defects. Panels a and b in ordered supercells. Panels c, d, e, f in $6P$ disordered supercells (table I).

being composed of 27 quasi identical signals. The names used to specify each eigenvector are the ones described in Refs. 30, 40, and 41. The Raman active tensors of the $R\bar{3}m$ space group have the forms [42]:

$$A_{1g} \qquad \begin{pmatrix} a & \cdot & \cdot \\ \cdot & a & \cdot \\ \cdot & \cdot & b \end{pmatrix}$$

$$E_{g_1} \qquad \begin{pmatrix} c & \cdot & \cdot \\ \cdot & -c & d \\ \cdot & d & \cdot \end{pmatrix}$$

$$E_{g_2} \qquad \begin{pmatrix} \cdot & -c & -d \\ -c & \cdot & \cdot \\ -d & \cdot & \cdot \end{pmatrix}$$

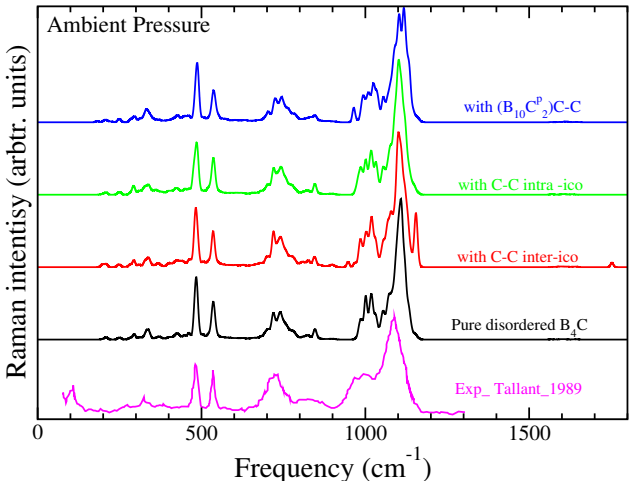

FIG. 9. Theoretical Raman spectra of the 3×3×3 rhombohedral supercell ($B_{11}C^p$)C-B-C at 0 GPa containing different kind of defects.

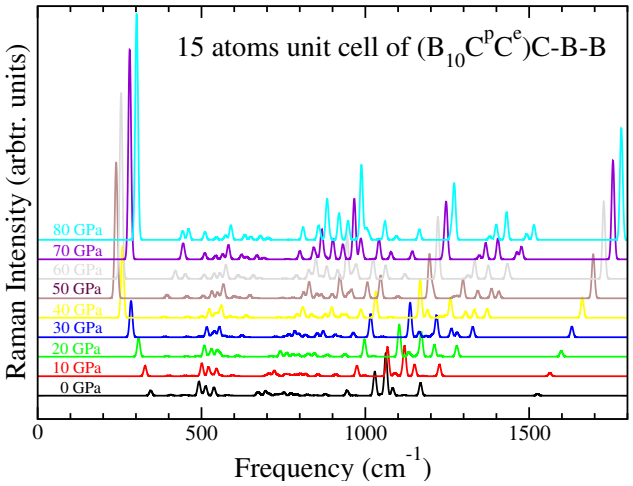

FIG. 10. Theoretical Raman spectra of the 15 atoms unit cell of ($B_{10}C^pC^e$)CBB from 0 to 80 GPa. The low frequency mode for which the Grüneisen parameter is negative below 50 GPa and positive above is the chain bending mode. The behavior of the mode intensity under pressure however does not explain the experimental observations [14].

In our calculations, the defective supercells are in space group $P1$ (#1), However, the *6P* disorder restores on average the $R\bar{3}m$ symmetry (space group #166), which is expressed by the "·" that are much smaller than in the matrix obtain for ordered systems. The averaged symmetry (A_{1g}, Eg,...) of a vibrational mode calculated in the $P1$ supercells is taken as the one of the vibrational mode on which it has the highest projection among all the ones calculated in a reference $R\bar{3}m$ supercell (containing only (B_{12})C-C-C unit cells) and for which the symmetries are well known.

The Raman intensity of each mode ν is calculated as

$$I^\nu \propto |\overrightarrow{P}_i \cdot \overleftrightarrow{A^\nu} \cdot \overrightarrow{P}_d|^2 \frac{1}{\omega_\nu}(n_\nu + 1) \tag{B1}$$

where $\overrightarrow{P_i}$ (resp. $\overrightarrow{P_d}$) is the incoming (resp. diffused) polarization, and $n_\nu = [e^{\frac{\hbar\omega_\nu}{k_B T}} - 1]^{-1}$ is the Bose-Einstein population of the ν-th phonon. The Raman tensor of the ν-th mode $\overleftrightarrow{A}^\nu$ is defined as [38]:

$$A^\nu_{lm} = \sum_{k\gamma} \frac{\partial^3 E^{el}}{\partial E_l \partial E_m \partial u_{k\gamma}} \frac{\mathrm{w}^\nu_{k\gamma}}{\sqrt{M_\gamma}} \tag{B2}$$

where E^{el} is the DFT total energy of the system, $u_{k\gamma}$ the atomic displacement of the γ-th atom in the k-th cartesian direction, E_l is the l-th cartesian component of a uniform electric field, M_γ the atomic mass and $\mathrm{w}^\nu_{k\gamma}$ the ν-th normal mode.

When experiments are performed on monocristals, the ratio of the A_{1g} and E_g intensities depends on the crystal orientation. However, the experimental orientation is generally not described in the literature. Hence, to be more general, we chose to show the polycrystalline averaged intensity, also averaged on the polarization in the most common back-scattering geometry:

$$\overline{I^\nu} = \frac{\int_0^\pi \int_0^{2\pi} \int_0^{2\pi} \int_0^{2\pi} I^\nu(\theta,\phi,\lambda,\mu) sin(\theta) \mathrm{d}\theta \mathrm{d}\phi \mathrm{d}\lambda \mathrm{d}\mu}{\int_0^\pi sin(\theta)\mathrm{d}\theta \int_0^{2\pi} \mathrm{d}\phi \int_0^{2\pi} \mathrm{d}\lambda \int_0^{2\pi} \mathrm{d}\mu} \tag{B3}$$

where θ and ϕ are variables related to crystal orientation and λ (resp. μ) describes all the possible incoming (resp. diffused) polarizations, orthogonal to the propagation vector. The development of Eq. B3 gives [43]:

$$\begin{aligned}\overline{I^\nu} = \frac{n_\nu + 1}{15\omega_\nu} [7 &\left(A^2_{xy} + A^2_{xz} + A^2_{yz}\right) \\ &+ 4\left(A_{xx} + A_{yy} + A_{zz}\right) \\ &+ A_{xx}A_{yy} + A_{xx}A_{zz} + A_{yy}A_{zz}]\end{aligned} \tag{B4}$$

In addition to the natural broadening coming from the polar disorder that slightly displaces the $5A_{1g}$+$7E_g$ lines in each of the 27 building-block cells, each peak has been enlarged using a Gaussian function for which the full width at half minimum (FWHM) is 10 cm^{-1}, value experimentally measured for the two narrow peaks (*pcr* and *lib* in figure 3).

Appendix C: Bond length contraction

The calculated bond-length contractions are in excellent agreement with the measured ones (figure 11, top panel). To compare them, we show the length contraction relative to the low pressure bond length (figure 11, bottom panel). The Grüneisen coefficients can be interpreted with four mains trends (table II).

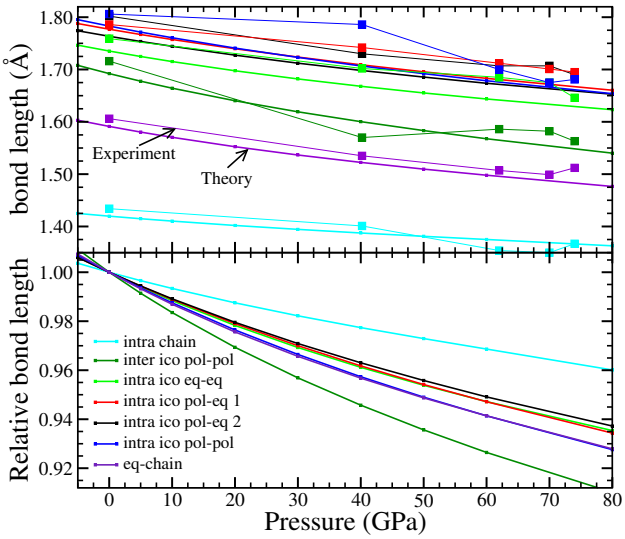

FIG. 11. Typical bond lengths in absolute (top panel) and relative (bottom panel) value as a function of pressure. Experiment from Ref. 14 (squares).

(i) The largest relative bond length reduction is the inter-icosahedral polar-polar one, and the corresponding vibrations (Inter-I Sym and Inter-I Asym in table II) consequently have the largest Grüneisen coefficients, all above 1.2 cm^{-1}/GPa.
(ii) The intermediate bond length reduction occurs for the intra-icosahedral bonds (Intra-I polar-polar, equatorial-polar and equatorial-equatorial bonds). The corresponding vibrations consequently have intermediate slopes around 0.9 cm^{-1}/GPa.
(iii) The smallest bond reduction occurs for the bonds between the atoms of the chain. However, the vibrations of the chain also depend on six other bonds with atoms in icosahedra (equatorial atom-chain atom bonds) that undergo the second biggest contraction under pressure, implying that Chain-Rot and Chain-Sym modes have large Grüneisen coefficient.
(iv) The libration of the icosahedron (*lib*) and the pseudo chain rotation (*pcr*) are not correlated to a bond stretching vibration, but to an angular vibration of the bonds surrounding respectively the icosahedra and the chains. They are consequently less impacted by the pressure: their Grüneisen coefficients are lower than 0.4 cm^{-1}/GPa.

Appendix D: Origin of the large broadening

The fact that the two low frequency peaks form a broad band is explained by the huge number of different environments that the flexured chain can have, each of them having its own frequency (figure 12): the 40 GPa low frequency peak is not always at the same position. For example, as explained in Sec. II A, three B_{12} icosahedra are needed to compensate the charge of the B-C-B-C defect. These three icosahedra can be located on each of the eight surrounding icosahedra, making $\binom{3}{8}$ possible environments. As another example, instead of the B-C-B-C chain, one could find a C-C-B-C chain surrounded by four (B_{12}) (figure 12, black spectra), which also induces a different position of the bending mode peak. Another example is the charged state of the defect (figure 12, green curve), that can goes up to 3+ when replacing the 3 (B_{12}) icosahedra by $B_{11}C^p$ ones. More generally, any interstitial atom will induce a similar behavior.

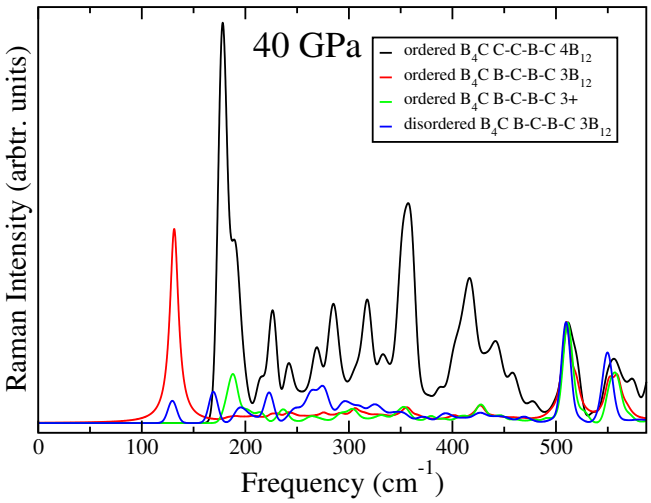

FIG. 12. Theoretical low frequency peak positions at 40 GPa for different defect configurations.

[1] V. Domnich, S. Reynaud, R. A. Haber, and M. Chhowalla, J. Am. Ceram. Soc. **94**, 3605 (2011).
[2] D. Bylander and L. Kleinman, Phys. Rev. B **43**, 1487 (1991).
[3] R. Lazzari, N. Vast, J. M. Besson, S. Baroni, and A. Dal Corso, Phys. Rev. Lett. **83**, 3230 (1999).
[4] R. Lazzari, N. Vast, J. Besson, S. Baroni, and A. D. Corso, Phys. Rev. Lett. **85**, 4194 (2000).
[5] K. Schwetz and P. Karduck, J. Less. Comm. Met. **175**, 1 (1991).
[6] P. Rogl, J. Vrestal, T. Tanaka, and S. Takenouchi, CALPHAD **44**, 3 (2014).
[7] A. Ektarawong, S. Simak, L. Hultman, J. Birch, and B. Alling, Phys. Rev. B **90**, 024204 (2014).
[8] D. Bylander, L. Kleinman, and S. Lee, Phys. Rev. B **42**, 1394 (1990).

[9] F. Mauri, N. Vast, and C. J. Pickard, Phys. Rev. Lett. **87**, 085506 (2001).

[10] K. Rasim, R. Ramlau, A. Leithe-Jasper, T. Mori, U. Burkhard, H. Borrmann, W. Schnelle, C. Carbogno, M. Scheffler, and Y. Grin, Ang. Chem. **130**, 1 (2018).

[11] G. Roma, K. Gillet, A. Jay, N. Vast, and G. Gutierrez, Phys. Rev. Mater. **5**, 063601 (2021).

[12] K. Shirai, K. Sakuma, and N. Uemura, Phys. Rev. B **90**, 064109 (2014).

[13] A. Jay, O. Hardouin Duparc, J. Sjakste, and N. Vast, J. App. Phys. **125**, 185902 (2019).

[14] A. Hushur, M. Manghnani, H. Werheit, P. Dera, and Q. Williams, J. Phys.: Cond. Matter. **28**, 045403 (2016).

[15] U. Kuhlmann, H. Werheit, and K. Schwetz, J. Alloys and Compo. **189**, 249 (1992).

[16] A. Jay, N. Vast, J. Sjakste, and O. Hardouin Duparc, Appl. Phys. Lett. **105**, 031914 (2014).

[17] E. Betranhandy, N. Vast, and J. Sjakste, Sol. St. Sc. **14**, 1683 (2012).

[18] J. Guo, L. Zhang, T. Fujita, T. Goto, and M. Chen, Phys. Rev. B **81**, 060102 (2010).

[19] X. Yan, Z. Tang, L. Zhang, J. Guo, C. Jin, Y. Zhang, T. Goto, J. W. McCauley, and M. W. Chen, Phys. Rev. Lett. **102**, 075505 (2009).

[20] I. Chuvashova, B. Gasharova, Y.-L. Mathis, L. Dubrovinsky, and N. Dubrovinskaia, J. Inorg. Gen. Chem. **643**, 1357 (2017).

[21] A. Chakraborti, A. Jay, O. Hardouin Duparc, J. Sjakste, K. Béneut, N. Vast, and Y. Le Godec, Acta Mater. , 117553 (2021).

[22] H. Werheit, Phys. Rev. Mater. **6**, 016601 (2022).

[23] G. Roma, A. Jay, N. Vast, O. Hardouin Duparc, and G. Gutierrez, Phys. Rev. Mater. **6**, 016602 (2022).

[24] H. Werheit, H. Rotter, H. Meyer, H. Hillebrecht, S. Shalamberidze, T. Abzianidze, and G. Esadze, J. Sol. St. Chem. **117**, 569– (2004).

[25] K. Shirai and N. Uemura, Sol. St. Sc. **14**, 1609 (2012).

[26] Y. He, Y. Shen, B. Tang, and Q. An, The Journal of Physical Chemistry C **127**, 2104 (2023).

[27] T. Sahu, A. Bhattacharyya, and A. Gandi, Physica B: Cond. Matt. **633**, 413738 (2022).

[28] H. Werheit, Phys. Rev. Mater. **6**, 016601 (2022).

[29] T. Sahu, A. Bhattacharyya, and A. Gandi, Physica B: Cond. Matt. **657**, 414781 (2023).

[30] A. Jay, *Conception in silico d'une nouvelle phase de carbure de bore*, Ph.D. thesis, École Polytechnique, Palaiseau, France (2015).

[31] K. Wade, Adv. Inorg. Chem. Radiochem. **18**, 1 (1976).

[32] P. Hohenberg and W. Kohn, Phys. Rev. **136**, B864 (1964).

[33] W. Kohn and S. L. J, Phys. Rev. **140**, A1133 (1965).

[34] J. P. Perdew and A. Zunger, Phys. Rev. B **23**, 5048 (1981).

[35] P. Giannozzi, O. Andreussi, T. Brumme, O. Bunau, M. B. Nardelli, M. Calandra, R. Car, C. Cavazzoni, D. Ceresoli, M. Cococcioni, N. Colonna, I. Carnimeo, A. D. Corso, S. de Gironcoli, P. Delugas, R. A. DiStasio, A. Ferretti, A. Floris, G. Fratesi, G. Fugallo, R. Gebauer, U. Gerstmann, F. Giustino, T. Gorni, J. Jia, M. Kawamura, H.-Y. Ko, A. Kokalj, E. Küçükbenli, M. Lazzeri, M. Marsili, N. Marzari, F. Mauri, N. L. Nguyen, H.-V. Nguyen, A. O. de-la Roza, L. Paulatto, S. Poncé, D. Rocca, R. Sabatini, B. Santra, M. Schlipf, A. P. Seitsonen, A. Smogunov, I. Timrov, T. Thonhauser, P. Umari, N. Vast, X. Wu, and S. Baroni, J. Phys.: Cond. Matter. **29**, 465901 (2017).

[36] H. Monkhorst and J. Pack, Phys. Rev. B **13**, 5188 (1976).

[37] S. Baroni, S. de Gironcoli, A. Dal Corso, and P. Giannozzi, Rev. Mod. Phys. **73**, 515 (2001).

[38] M. Lazzeri and F. Mauri, Phys. Rev. Lett. **90**, 036401 (2003).

[39] H. Werheit, Ceram. Engin. Sc. Proc. **35**, 87 (2014).

[40] N. Vast, S. Baroni, G. Zérah, J. M. Besson, A. Polian, M. Grimsditch, and J. C. Chervin, Phys. Rev. Lett. **78**, 693 (1997).

[41] N. Vast, *Propriétés vibrationnelles du bore α et du carbure de bore B_4C*, Ph.D. thesis, Université Paris VI, France (1998).

[42] H. Poulet and J. Mathieu, *Vibration spectra and symmetry of crystals* (Gordon and Breach, New York, 1976).

[43] E. Spanò and M. Bernasconi, Phys. Rev. B **71**, 174301 (2005).